

Supporting Information for

Approaching the Collection Limit in Hot Electron Transistor with Ambipolar Hot Carrier Transport

*Wei Liu,^{1, ‡} Lingfei Li,^{1, ‡} Hongwei Guo,¹ Akeel Qadir,¹ Srikrishna Chanakya Bodepudi,¹ Khurram Shehzad,¹ Whenchao Chen^{1, 2}, Ya-Hong Xie,³ Xiaomu Wang,^{4, *} Bin Yu,¹ and Yang Xu^{1, 2, *}*

¹College of Information Science and Electronic Engineering, College of Microelectronics, Zhejiang Key Laboratory for Advanced Microelectronic Intelligent Systems and Applications, ZJU Micro-Nano Fabrication Center, Zhejiang University, Hangzhou 310027, China

²Zhejiang University/University of Illinois at Urbana-Champaign Institute, Haining 314400, China

³Department of Materials Science and Engineering, University of California, Los Angeles, CA 90095, USA

⁴National Laboratory of Solid State Microstructures, School of Electronic Science and Engineering, Collaborative Innovation Center of Advanced Microstructure, Nanjing University, Nanjing 210093, China.

1. Modelling of hot holes and hot electrons transport

The current flow I through a tunneling junction is described by Landauer formula^{1, 2}

$$I \propto \int DOS_1(E + qV)DOS_2(E)T(E)(f(E + qV) - f(E))dE \quad S1$$

Where E , DOS , T , f , and V are the energy of carriers, density of states, transmission probability, Fermi-Dirac distribution and voltage bias applied to the junction, respectively.

In our devices, multi-layer (several nanometer) and fewer-layer (~ 1 nm) graphene are used as emitter and base materials, respectively. We treat the MLG and FLG as three dimensional and two-dimensional Dirac system, respectively. The DOS for emitter (MLG) and base (FLG) are modelled as

$$DOS_E = 8\pi m^* \sqrt{2m^* E}/h^3 \quad S2$$

and

$$DOS_B = 8\pi E/h^2 v^2 \quad S3$$

where m^* , h , v , and E are the effective mass of carriers, Plank constant, Fermi velocity of carriers in graphene and the energy level of carriers, and the subscripts E and B represent emitter and base. We employ piecewise function $T(E)$ calculated by Ma, Q *et al.*² using Wentzel-Kramers-Brillouin (WKB) method.

When the emitter is positively biased ($V_{EB} > 0$), the holes that transmit from emitter to base and electrons that transmit from base to emitter can be described as

$$I \propto \int DOS_E(E + qV_{EB})DOS_B(E)T(E)(f(E) - f(E + qV_{EB}))dE \quad S4$$

When the emitter is negatively biased ($V_{EB} < 0$), the electrons that transmit from emitter to base and holes transmit from base to emitter can be described as

$$I \propto \int DOS_E(E + qV_{EB})DOS_B(E)T(E)(f(E + qV_{EB}) - f(E))dE \quad S5$$

Where V_{EB} is the voltage bias applied to the emitter-base junction.

To distinguish between the hole and electron current components, we integrate equation S4 and S5 at different energy range. We set Fermi level of graphene in base 0.1 eV below the Dirac point as graphene used is usually p-doped. This Fermi level at the base is set as energy reference, and we calculate electron current at positive energy range and hole current at negative energy range as shown in Figure S1.

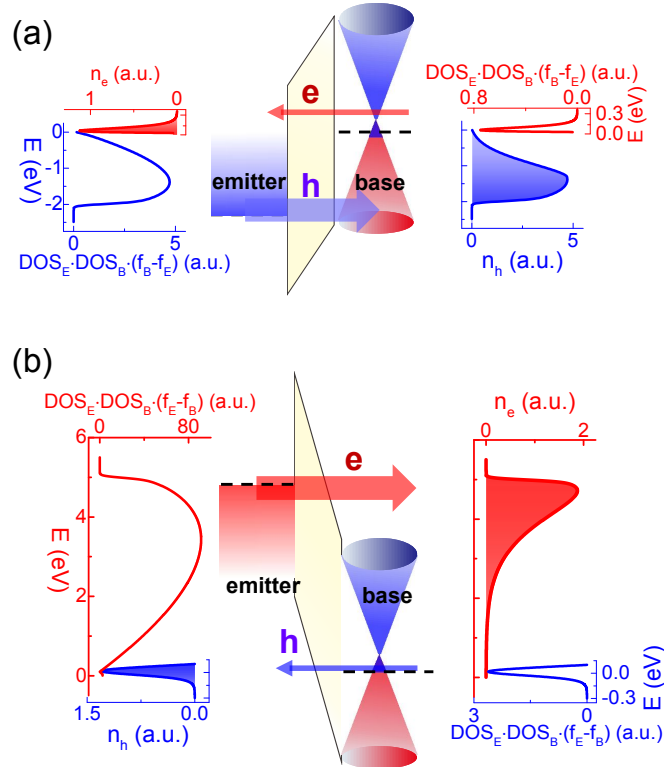


Figure S1. Calculations for the carrier transport in MLG/hBN/FLG heterostructure. (a) positive and (b) negative bias condition. The n_e , n_h , and f are the number of electrons, number of holes, and Fermi-Dirac distribution, respectively. The emitter and base are modelled by parabolic and linear DOS, corresponding to the MLG and FLG, respectively. The transmitted carrier density is calculated and its values are normalized.

2. Images and two-terminal test of HET with thicker hBN

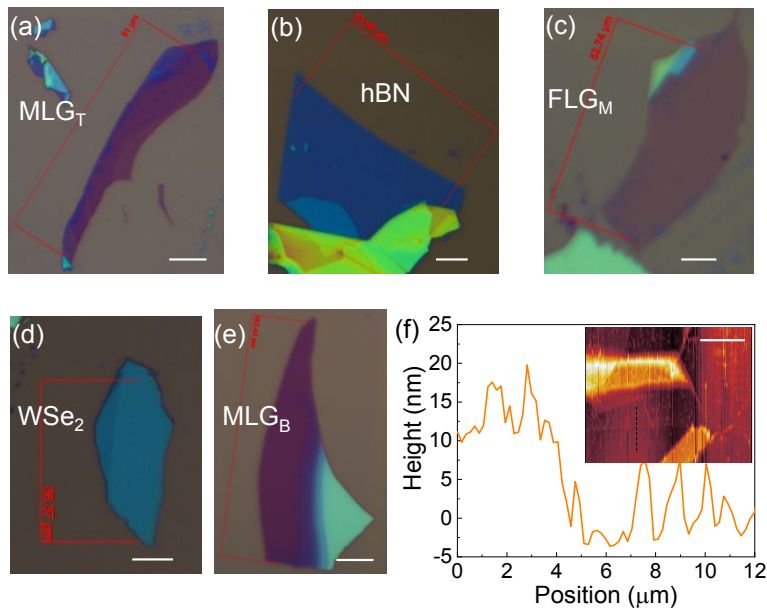


Figure S2. OM images of each layer and AFM image of hBN in the vdW HET with thick hBN.

Scale bar: 10 μm.

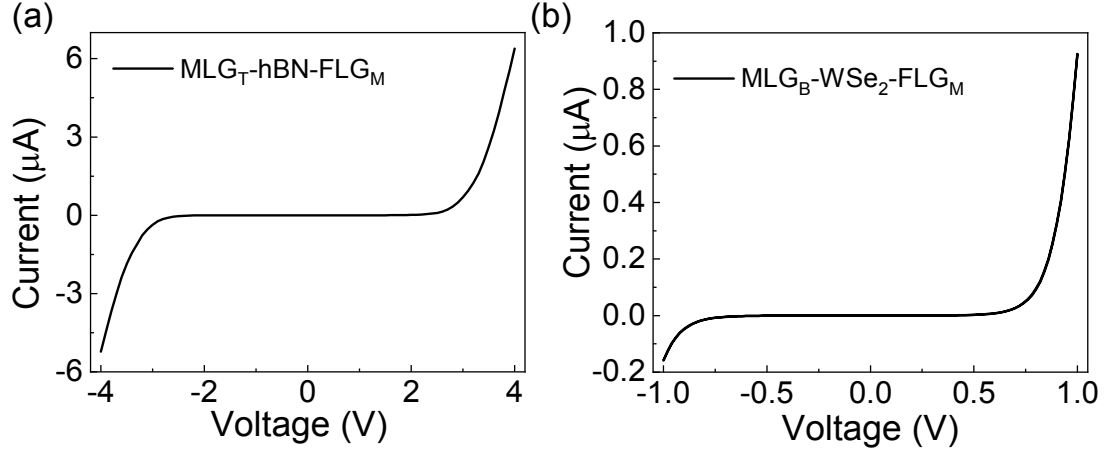


Figure S3. Two terminal test of the vdW HET with thicker hBN. The IV curve is measured in the two single junctions: top-layer MLG to middle-layer FLG (a) and bottom-layer MLG to middle-layer FLG (b).

We show the optical microscope (OM) image of each layer and height profile of hBN measured by atomic force microscopy (AFM) in Figure S2. From the optical contrast we can estimate a thickness of WSe_2 at ~ 10 nm and that of graphene within 1 nm. The AFM measurement on the exposed hBN layer in the fabricated device shows its thickness of 10~15 nm.

The two-terminal test of this device is shown in Figure S3. We can see an asymmetric behavior in the $\text{MLG}_B\text{-WSe}_2\text{-FLG}_M$ junction. When this junction is used as emitter junction (V_E applied on MLG_B), the V_E needed to drive a electron current (negative bias) is bigger than that to drive a hole current (positive bias) of the same value. This can explain why electrons have smaller collector voltage V_{CB} than holes when emitter current is same in Figure 2 of the main text. In the Figure 2a, b, we apply constant current on the emitter-base junction. But the $\text{MLG/WSe}_2\text{/FLG}$ junction show asymmetric behavior due to the asymmetry between MLG and FLG, which can be seen in Supporting Information Figure S3b. This asymmetry in the IV curve of the junction

results in a larger voltage bias in the negative I_E than in positive I_E (same absolute value of I_E) when bias is applied on the MLG. So the carriers in Figure 2b have higher injection energy than that in Figure 2a due to the larger voltage bias.

3. AFM and OM image of HET with thinner hBN and its two-terminal test, base current, emitter voltage bias and base-floating data

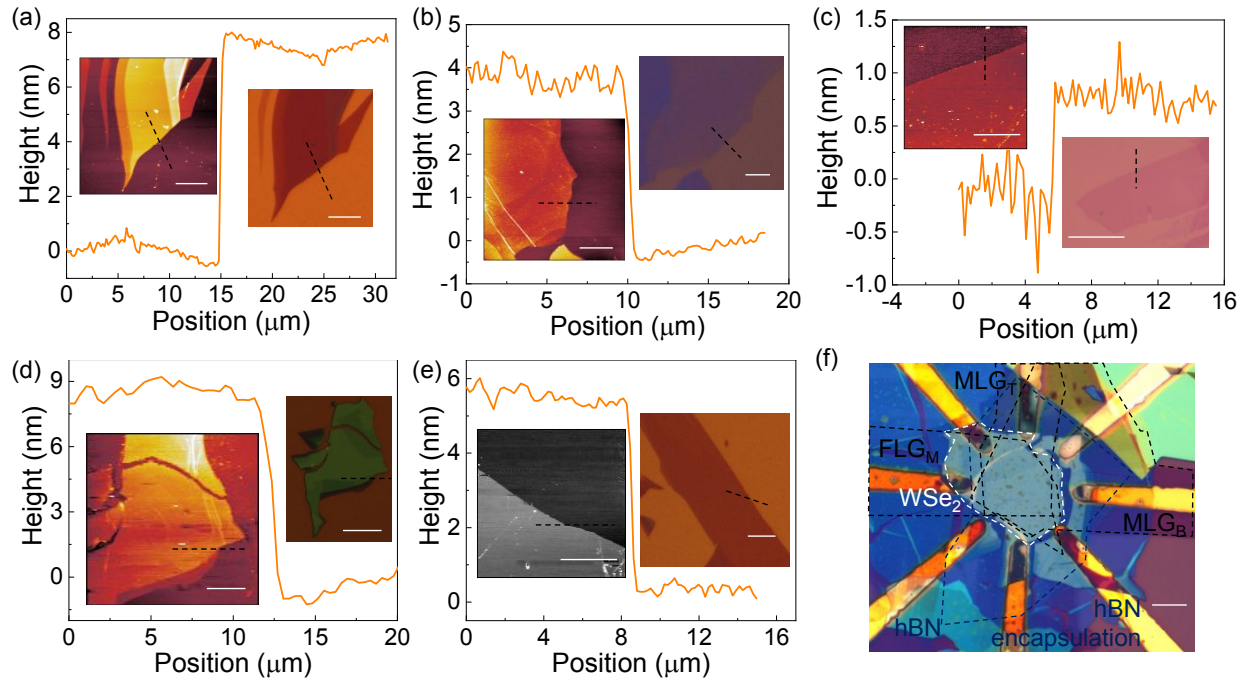


Figure S4. AFM and OM images of each individual layer in the vdW HET with thinner hBN and the OM image of the stacked device. Scale bar: 10 μm . The AFM images show the thickness of each layer in the HET is 8 nm, 4 nm, 1 nm, 9 nm and 6 nm for top MLG, hBN, FLG, WSe₂, and bottom MLG, respectively.

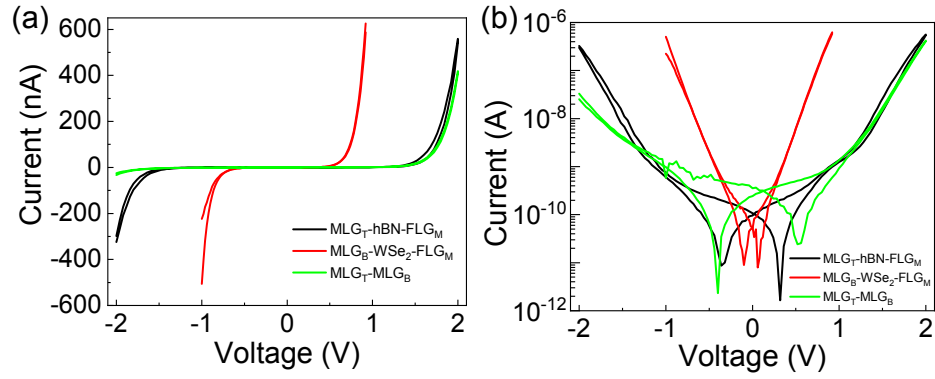


Figure S5. Two terminal test of the vdW HET with thinner hBN in linear (a) and logarithmic (b) scale.

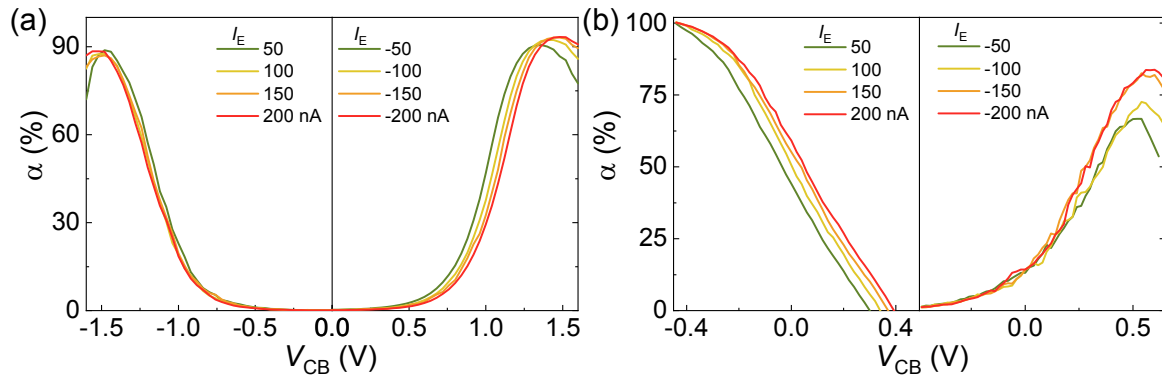


Figure S6. Collection efficiency of the vdW HET with thinner hBN in WSe₂ EBB/ hBN BCB (a) and hBN EBB/WSe₂ BCB (b) bias condition.

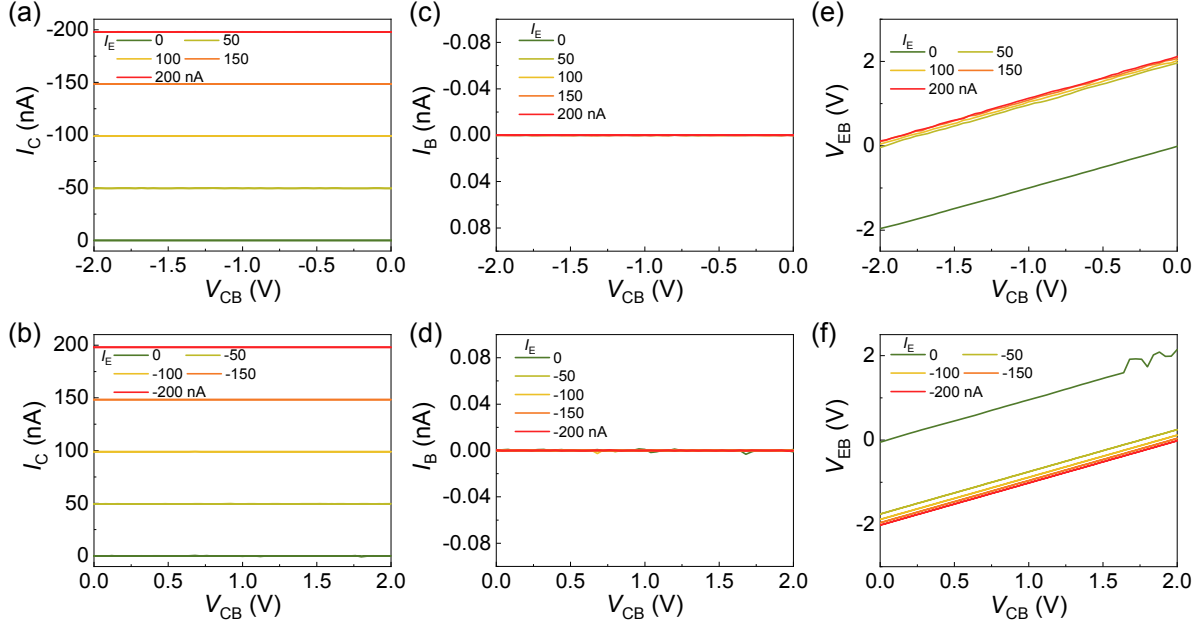


Figure S7. Base-floating test. Common-base output curves of the vdW HET biased in WSe₂ EBB/ hBN BCB condition: collector current I_C (a, b), base current I_B (c, d), and emitter voltage bias V_{EB} (e, f) in hot electron and hot hole mode.

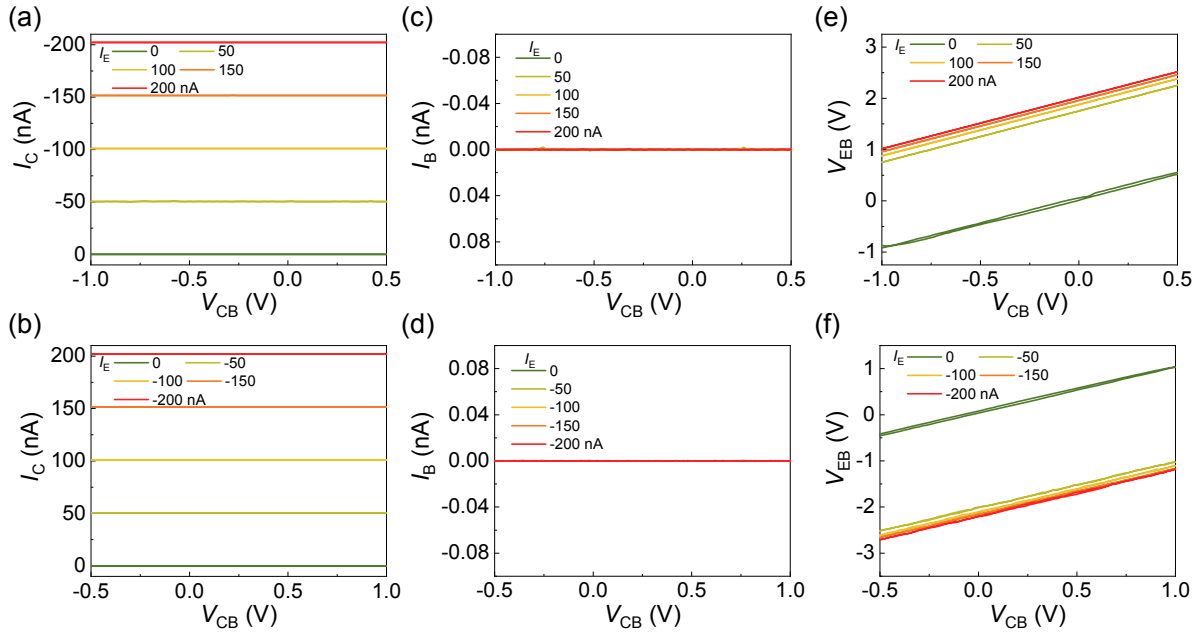


Figure S8. Base-floating test. Common-base output curves of the vdW HET with thinner hBN biased in hBN EBB/WSe₂ BCB condition: collector current (a, b), base current (c, d), and emitter voltage bias (e, f) in hot electron and hot hole mode..

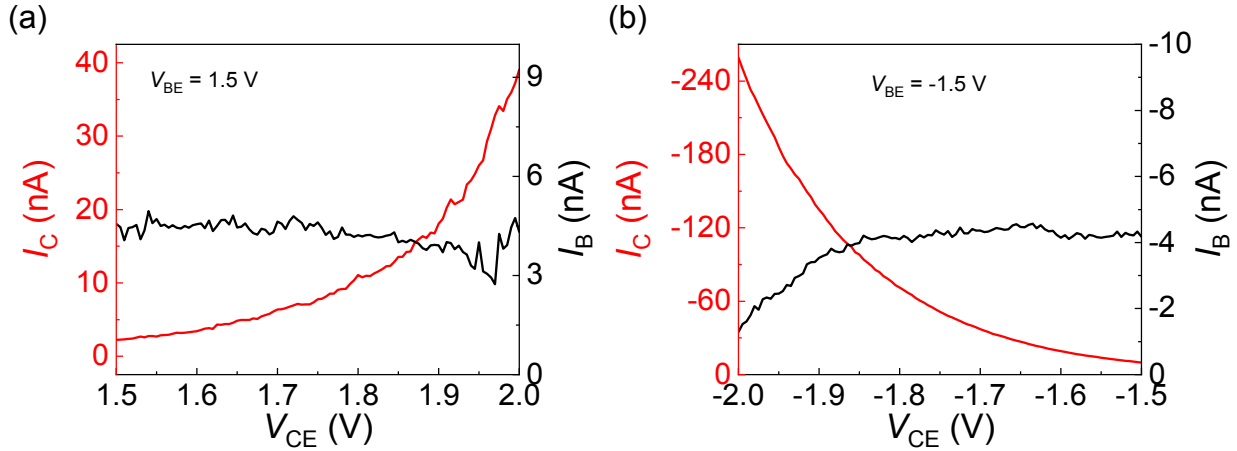


Figure S9. Common emitter output curves of the vdW HET with thinner hBN in hot-h (a) and hot-e (b) mode with WSe₂ EBB/ hBN BCB bias condition.

We present systematic study including AFM and OM image, two-terminal test, base floating test, and common emitter test on the vdW HET with thinner hBN to better understand the nature of carrier transport.

The two-terminal test of the single junctions shows a typical tunneling behavior. The small hysteresis indicates the good junction quality. In this device, we get maximum collection efficiency of 88.9% and 93.3% for holes and electrons in WSe₂ EBB/ hBN BCB and close to 100% and 83.8% for holes and electrons in hBN EBB/ WSe₂ BCB condition. We note that the calculated collection efficiency may be affected by field-effect modulation of the base-collector junction. The V_E not only injected hot carriers but also tune the base-collector junction, adding more current in the hot-h part and suppressing current in the hot-e part.

When we float the base and keep other parameters unchanged (Figure S7-S8, constant current I_E applied to the emitter and sweeping voltage V_C bias applied to the collector), we see a dramatically different phenomenon. The collector current is always a constant value in the base-floating test which equals to the emitter current and there is no off state, saturation and leakage region in the I_C - V_C curve. The I_B is always zero because of the floating condition. The emitter voltage changes linearly with increasing V_C . In the base-floating test, the device behaves like a two-terminal resistor, which is totally different from the three-terminal common-base test.

We present the common-emitter output curve in Figure S9. We extract the current gain β at a voltage before which I_B is not affected by the leakage current of the base-collector junction. We got $\beta \sim 10$ at $V_{CE} = 2V$ and $\beta \sim 15$ at $V_{CE} = -1.8V$ when operating at hot-h and hot-e mode, respectively. We don't observe saturation region in common-emitter curves of the vdW HET as in traditional bipolar junction transistor (BJT) devices. As we know, BJT is formed by two pn junctions which turn on at positive bias and turn off at reverse bias. So BJT works at the condition with forward-biased emitter-base junction and reversed-biased base-collector junction. With rectification property in the base-collector junction, BJT can collect carriers with negligible leakage at the reverse-biased base-collector junction. In HET, however, the emitter and collector are formed by tunneling junctions, which turn on at both forward and reverse bias. So HET cannot get good transfer curve when working at common-emitter condition because the change of V_B will change bias on the base-collector junction and lead to large modulation on background current (This will not happen in BJT because the reverse current saturates in base-collector pn junction). And in output curve, the increase of V_C increases leakage current through base-collector junction, and changes I_B at large bias value.

We note that the device is not perfect now, additional work need to be done in the future to solve this problem and drive it to real application. Although the vdW HET does not work well in common emitter bias condition, it still provides powerful platform for the study of hot carrier dynamics and transport.

4. HET with symmetric barriers

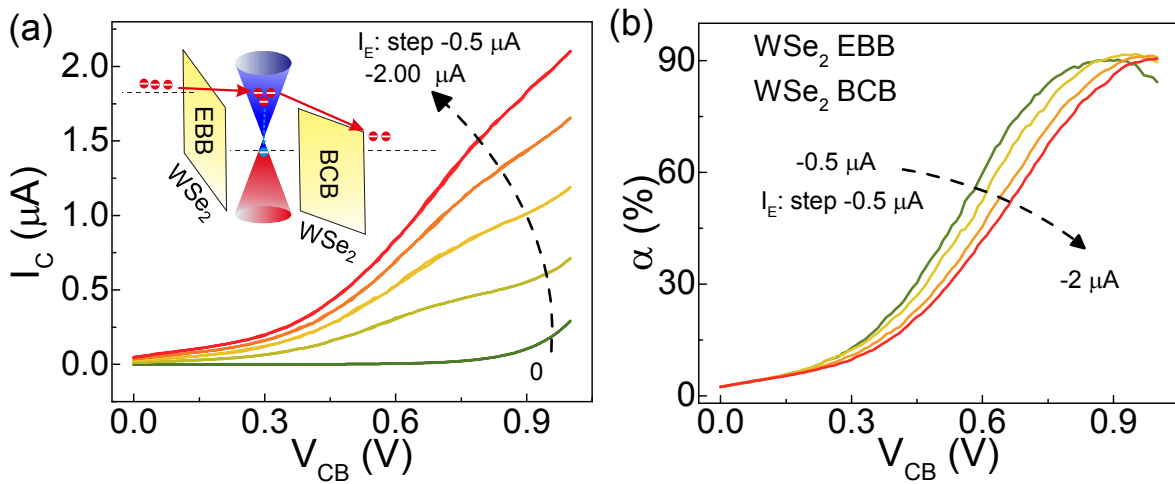


Figure S10. Output characteristics of HET with symmetric barriers. (a) Output collector current as a function of base-collector bias at different injection current. (b) Calculated collection efficiency from (a).

We fabricated symmetric HETs with WSe₂ as the emitter-base barrier (EBB) and base-collector barrier (BCB). The output curves are shown in Figure S10. The band diagram is shown in the inset.

5. Summary of efficiency in HETs with different barriers

We reproduced the results presented in the main text in twelve asymmetric and two symmetric devices and summarized the maximum efficiencies in Figure S2. Nine asymmetric HETs show record efficiencies approaching the theoretical limit of 100% under hBN EBB/WSe₂ BCB bias condition, and 70% ~ 98% under WSe₂ EBB/hBN BCB bias condition. Other three asymmetric HETs show lower collection efficiencies of 85% ~ 95% under hBN EBB/WSe₂ BCB bias condition and similar values under opposite bias condition. HETs with symmetric WSe₂ EBB/ WSe₂ BCB barriers show 85% ~ 95% collection efficiencies. We pick up two asymmetric devices with close to 1 collection efficiency and proper overlapping condition discussed in Supporting Information 6 and show the data in Figure S13.

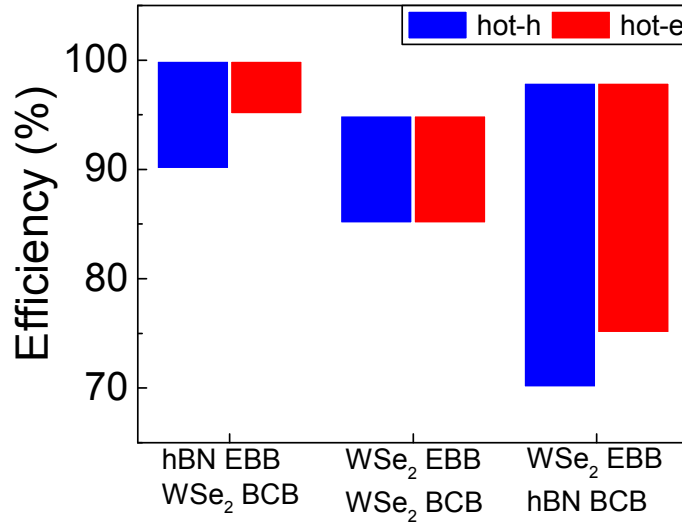


Figure S11. Efficiencies of HET with different barriers. It is worth noting that even with the thin hBN as EBB we can collect hot carriers at zero V_{CB} , from which we speculate that the energy of injected hot carriers is still higher than the WSe₂ barrier. We define the voltage at which collector current decreases to zero as turn-off voltage V_{off} , and summarize the V_{off} as a function of hBN thickness in Figure S4. The V_{off} increases as hBN becomes thicker, as higher-energy

carriers is generated in the thicker hBN when injecting hot carriers (as illustrated in the inset of Figure S4 (c)). Thus, we can tune the V_{off} value by choosing proper hBN thickness to meet various demands in different applications.

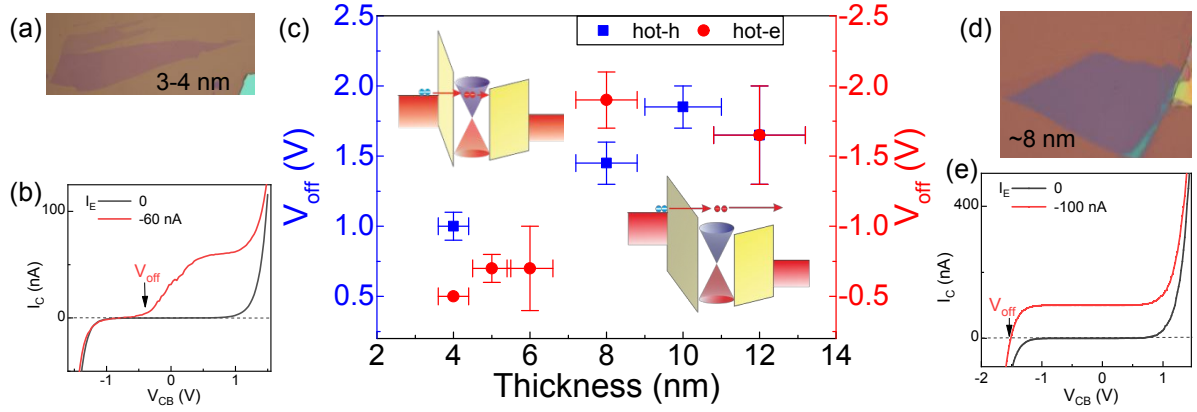


Figure S12. HETs with different thickness of hBN as EBB. (a) Optical image of a thinner hBN (3 ~ 4 nm) used in the HET. (b) Output curves of the HET with thinner hBN in (a) as EBB. (c) Turn-off voltage V_{off} as a function of the thickness of hBN in hBN EBB/WSe₂ BCB bias condition. Hot holes and hot electrons are represented by blue rectangles and red circles, respectively. Inset shows the band diagrams. (d) Optical image of a thicker hBN (~8 nm) used in the HET. (e) Output curves of the HET with thicker hBN in (c) as EBB.

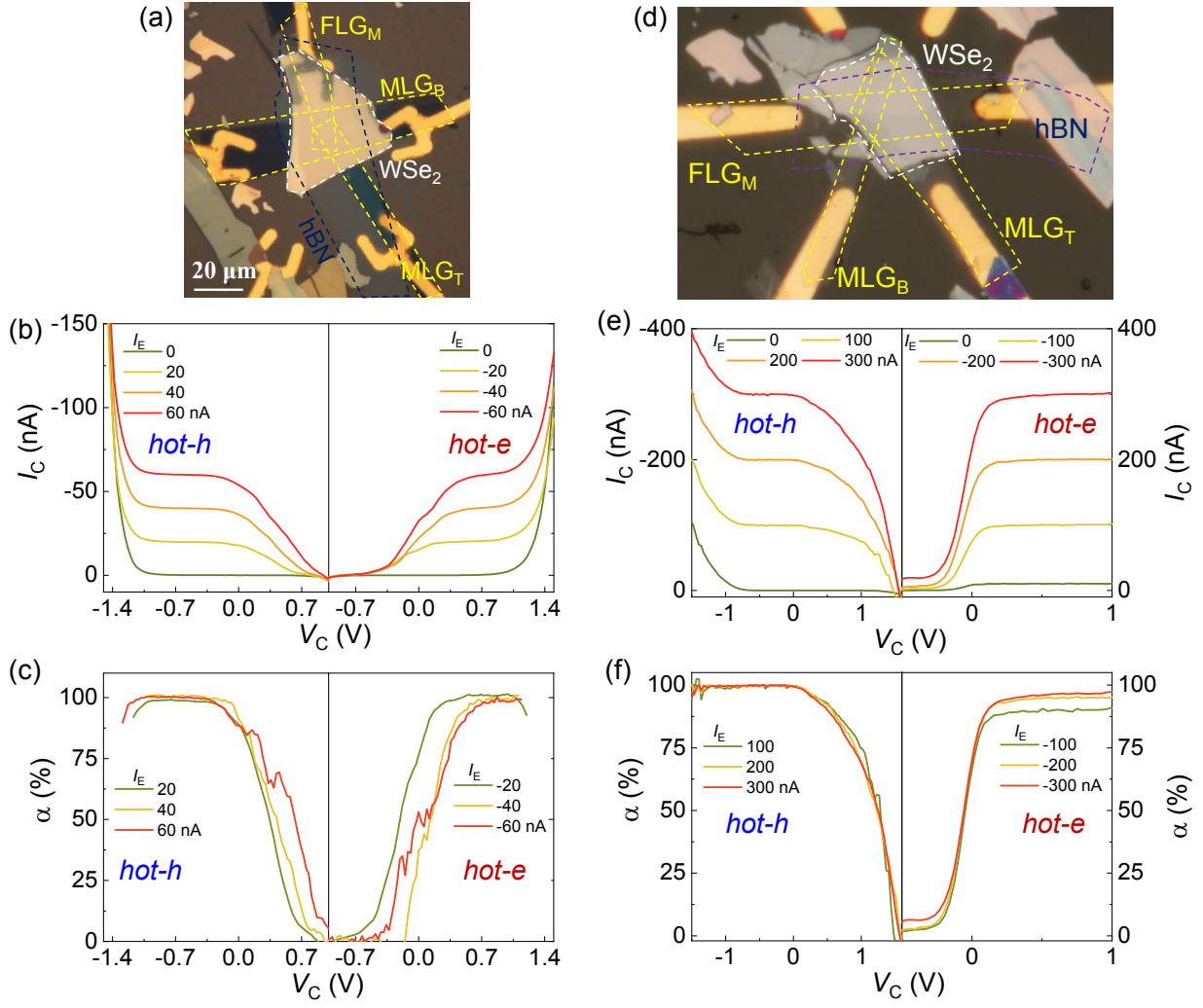


Figure S13. Other two devices with collection efficiency approaching unit. Their OM images (a) and (d), output curves (b) and (e), collection efficiency (c) and (f) measured in hBN EBB/WSe₂ BCB configuration.

6. Collection efficiency calculation considering overlapping issue

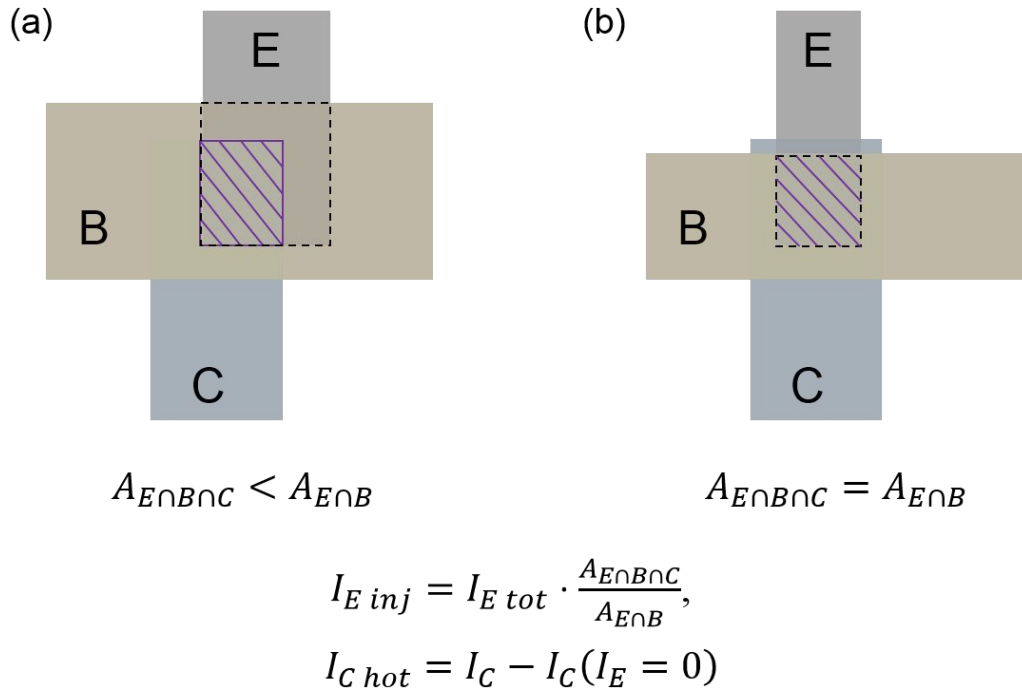


Figure S13. Schematics of two different overlap types. (a) overlap region $A_{E \cap B \cap C} < A_{E \cap B}$, (b) overlap region $A_{E \cap B \cap C} = A_{E \cap B}$. The area in the dashed line is the overlap between the emitter and base ($A_{E \cap B}$) and the area in the shadow is the overlap among the emitter, base and collector ($A_{E \cap B \cap C}$).

To get high-quality van der Waals heterojunctions we use mechanically exfoliated 2D materials which are usually of random shape and size. In the fabrication process, we try to pick up 2D layers with rectangular shape and align them with great care to make the three graphene layers well overlapped. There is some misalignment between every two of the three graphene layers because of the randomness of the exfoliated 2D materials. Fortunately, we can eliminate the errors contributed by the misalignment when calculating the emitter and collector currents by choosing specific pattern of the device

The overlapping area of the three graphene layers ($E \cap B \cap C$) is the effective channel area for hot carriers' transport. The area overlapped between two graphene layers but don't overlap with the third one ($E \cap B - E \cap B \cap C$ or $B \cap C - E \cap B \cap C$) will contribute to the leakage current. In the collector, fortunately, we can subtract the leakage current to get the collected hot carrier current by $I_{C\ hot} = I_C - I_C(I_E = 0)$. In the emitter, we calculate the effective injected current by $I_{E\ inj} = I_{E\ tot} \cdot \frac{A_{E \cap B \cap C}}{A_{E \cap B}}$, where $I_{E\ inj}$, $I_{E\ tot}$ are the effective injection current and total emitter current, respectively. By measuring the overlapping areas under optical microscope, we can estimate the value of the effective injection current. This may introduce some errors due to the estimation of the areas when $A_{E \cap B \cap C} < A_{E \cap B}$ (Figure S13 a), but will get accurate value when $A_{E \cap B \cap C} = A_{E \cap B}$ (Figure S13 b) because in this case all the I_E is injected into the effective device region. In this work, we make our main conclusions from the devices with $A_{E \cap B \cap C} = A_{E \cap B}$.

	Refs. [3-4]	Ref. [5]	Ref. [6]	Our previous work [7]	This work
Structure	Si/SiO ₂ /Gr/ Oxide/metal	Si/SiO ₂ /MoS ₂ / Oxide/ITO	Au/GaN/AlN/ Gr/WSe ₂ /Au	Gr/BN/Gr/WSe ₂ /Gr	MLG/hBN/FL G/WSe ₂ /MLG
Maximum α (%)	6.5	95	75	99.95	99.98
Current density (A/cm²)	$\sim 5 \times 10^{-5}$	$\sim 10^{-6}$	~ 50	~ 233	~ 400
Current saturation	N/A	N/A	✓	✓	✓
Ambipolar	N/A	N/A	N/A	N/A	✓
Lossless carrier transport	N/A	N/A	N/A	N/A	✓
Flexibility	N/A	N/A	N/A	N/A	✓

Table S1. The key performance of this work compared to previous studies.

Table S1 gives the comparison of our devices with related works³⁻⁷.

REFERENCES

1. Britnell, L.; Gorbachev, R. V.; Jalil, R.; Belle, B. D.; Schedin, F.; Mishchenko, A.; Georgiou, T.; Katsnelson, M. I.; Eaves, L.; Morozov, S. V.; Peres, N. M.; Leist, J.; Geim, A. K.; Novoselov, K. S.; Ponomarenko, L. A. Field-Effect Tunneling Transistor Based on Vertical Graphene Heterostructures. *Science* **2012**, 335, 947-950.
2. Ma, Q.; Andersen, T. I.; Nair, N. L.; Gabor, N. M.; Massicotte, M.; Lui, Chun H.; Young, A. F.; Fang, W.; Watanabe, K.; Taniguchi, T.; Kong, J.; Gedik, N.; Koppens, F. H. L.; Jarillo-Herrero, P. Tuning Ultrafast Electron Thermalization Pathways in a van der Waals Heterostructure. *Nat. Phys.* **2016**, 12, 455-459.
3. Vaziri, S.; Lupina, G.; Henkel, C.; Smith, A. D.; Ostling, M.; Dabrowski, J.; Lippert, G.; Mehr, W.; Lemme, M. C. A Graphene-Based Hot Electron Transistor. *Nano Lett.* **2013**, 13, 1435-1439.
4. Zeng, C.; Song, E. B.; Wang, M.; Lee, S.; Torres, C. M., Jr.; Tang, J.; Weiller, B. H.; Wang, K. L. Vertical Graphene-Base Hot-Electron Transistor. *Nano Lett.* **2013**, 13, 2370-2375.
5. Torres, C. M., Jr.; Lan, Y. W.; Zeng, C.; Chen, J. H.; Kou, X.; Navabi, A.; Tang, J.; Montazeri, M.; Adleman, J. R.; Lerner, M. B.; Zhong, Y. L.; Li, L. J.; Chen, C. D.; Wang, K. L. High-Current Gain Two-Dimensional MoS₂-Base Hot-Electron Transistors. *Nano Lett.* **2015**, 15, 7905-7912.
6. Zubair, A.; Nourbakhsh, A.; Hong, J.-Y.; Qi, M.; Song, Y.; Jena, D.; Kong, J.; Dresselhaus, M.; Palacios, T. Hot Electron Transistor with van der Waals Base-Collector Heterojunction and High-Performance GaN Emitter. *Nano Lett.* **2017**, 17, 3089-3096.
7. Guo, H.; Li, L.; Liu, W.; Sun, Y.; Xu, L.; Ali, A.; Liu, Y.; Wu, C.; Shehzad, K.; Yin, W.; Xu, Y. All-Two-Dimensional-Material Hot Electron Transistor. *IEEE Electron Device Lett.* **2018**, 39, 634-637.